Boundary-Layer Meteorology (2026) 192:14
https://doi.org/10.1007/s10546-025-00958-1

RESEARCH ARTICLE

Applying a Surface Heat Flux with Temporal Gradient to Large-Eddy Simulations of the Stable Boundary Layer

Lukas Bührend[1] · **Antonia Englberger**[1]

Received: 3 July 2025 / Accepted: 12 December 2025

Abstract
The impact of the lower boundary condition for potential temperature is investigated in idealized large-eddy simulations of the stable boundary layer. The numerical simulations are conducted by the flow solver EULAG (Eulerian/semi-Lagrangian fluid solver) using a non-linear forward-in-time advection scheme. While focusing on the moderately stable inter-comparison case GABLS1 of the GEWEX Atmospheric Boundary Layer Study initiative as a benchmark, the simulations are performed with a lower potential-temperature boundary condition prescribed by a surface heat flux rather than the more commonly applied time-dependent surface temperature. A negative surface heat flux increasing in magnitude with time successfully reproduces the benchmark results, whereas, a constant surface heat flux leads to temperature decoupling, a shallower boundary layer and a weaker low-level jet. In addition, the sensitivity of the results towards three subgrid-scale models (Deardorff-Schumann, Anisotropy, Nonlinear Backscatter) and various grid resolutions (12.5 m - 2 m) is analyzed. A crucial factor is the amount of the vertical turbulent transport in the numerical model, which is significantly influenced by the applied advection scheme and the SGS model. Further, the selected SGS model influences the energy spectrum by affecting the spatial range of eddy sizes.

Keywords Grid sensitivity · Large-eddy simulation · Stable boundary layer · Subgrid-scale model · Surface heat flux

1 Introduction

With the transition from the convective boundary layer during daytime to the stable boundary layer (SBL) at night, surface cooling leads to a rapid reduction of vertical mixing, assuming calm winds and no large geostrophic forcings. As a result, turbulence in the SBL is typically weak and anisotropic (Mahrt 2014). Further characteristics of the SBL are an

✉ Lukas Bührend
lukas.buehrend@dlr.de

[1] Deutsches Zentrum für Luft- und Raumfahrt, Institut für Physik der Atmosphäre, Oberpfaffenhofen, Germany

Published online: 12 January 2026

increase in potential temperature with height; a change in wind direction with altitude (wind veer) due to the predominance of the Coriolis force (Ekman spiral); and a super-geostrophic wind speed in the upper part of the boundary layer, called low-level jet (LLJ) (Stull 1988; Shapiro and Fedorovich 2010). Commonly, the SBL is subdivided into the weakly (or moderately) stable regime (wSBL) with continuous turbulence and a well-defined boundary layer height and the very stable regime (vSBL) with strong stratification and weak, intermittent turbulence (Mahrt 2014).

Idealized numerical simulations of the turbulent flow and the temporal evolution of the temperature field provide a valuable contribution to enhance our understanding of the complex interplay among these various SBL phenomena. In idealized simulations, these fields are undisturbed by mesoscale influences which facilitates parameter studies, as causes and effects of parameter changes are easily discernible.

The spatial and temporal scales of the simulation should be selected to adequately resolve turbulence, while maintaining reasonable computational cost and time. Large-eddy simulations (LESs) are a suitable approach here, as they resolve the energy-containing turbulent eddies in the atmospheric boundary layer via the filtered Navier–Stokes equation for momentum and the equation for potential temperature, density and other scalar quantities ("governing equations"). Turbulent eddies larger than the filter size Δ are directly resolved, whereas the subgrid-scale (SGS) model parametrizes turbulence with a characteristic length scale smaller than Δ. Here, the governing equations are resolved using the finite-difference fluid solver EULAG (Eulerian/semi-Lagrangian fluid solver, Prusa et al. 2008).

The small-scale and weak turbulent kinetic energy (*TKE*) under stable conditions (compared to neutral or convective cases) leads to heightened sensitivity of numerous factors. This includes surface boundary conditions for wind and potential temperature, the utilized solver and numerical settings like grid size, the advection scheme and the SGS model. Even when applying the same initial and boundary conditions in different models, results may vary quite significantly, as visible in a major inter-comparison of wSBL-LES by the first GABLS (GEWEX Atmospheric Boundary Layer Study) initiative in Beare et al. (2006) (from here on GABLS1). A detailed description of initial and boundary conditions for GABLS1 is given below in Sect. 2.4 and in Beare et al. (2006).

GABLS1 has served as a benchmark of a moderately SBL for numerous subsequent publications. A short review of some is given below. In this study, we focus on the following topics, where we see a requirement for further investigations:

(a) The influence of different surface heat flux boundary conditions (hfbcs) on the simulation results,
(b) The sensitivity of the hfbc towards the SGS model and
(c) The sensitivity of the hfbc towards the grid size.

(a) What effect do different hfbcs have on the simulated weakly stable boundary layer?

All participants of GABLS1 use the prescription of a constant cooling rate (i.e. linear decrease of surface temperature with time) as a lower boundary condition, i.e., a a cooling rate boundary condition (crbc) for potential temperature (Beare et al. 2006). Also subsequent publications referencing GABLS1 apply this crbc (e.g., Sullivan et al. 2016; Maronga and Li 2021; Maroneze et al. 2023). Typically, a larger cooling rate leads to a shallower SBL

height associated with a decrease of the height of the LLJ and a reduction of the *TKE* at all heights (Sullivan et al. 2016).

An alternative to defining the surface temperature over time is the prescription of a surface heat flux. When prescribing the lower boundary condition in this manner, the surface temperature becomes a dynamic variable and its temporal evolution is subject to turbulent forcings. To our knowledge, only Jiménez and Cuxart (2005) and Zhou and Chow (2011) apply a heat flux as a lower boundary condition for potential temperature in nighttime situations. Both studies set a constant or step-wise constant surface heat flux with time. However, it remains unclear how in detail the surface temperature evolves over time given this hfbc. To study this evolution, we set up the GABLS1 benchmark with both a constant and time-dependent surface heat flux.

In general, the lower boundary condition is a crucial issue in all atmospheric models: the effect of friction at the surface has to be parameterized, as it determines the heat transfer via the surface, influencing the lowest layer attached to the surface, which is typically not resolved in LES models. Almost all flow solvers, including (Jiménez and Cuxart 2005) and Zhou and Chow (2011), apply a constant flux layer to treat the roughness sub-layer in the model, using Monin-Obukhov Similarity Theory (MOST). As far as we are aware, the model EULAG developed by Smolarkiewicz and Margolin (1997) and the model used by Epifanio (2007) are the only ones where the drag coefficient is specified via the bulk formula as an empirical constant and the application of a constant flux layer is omitted. The influence of the type of lower boundary condition in the weakly stable GABLS1 case is currently under investigation in EULAG by Englberger et al. (2026). Both the approach using MOST and the direct specification of the drag coefficient can be applied equivalently. Here, we focus specifically on the hfbc.

Accordingly, EULAG offers a suitable testbed to investigate the impact of different hfbcs for potential temperature instead of applying a crbc (in conjunction with an empirical constant for the parameterization of the surface drag) for the GABLS1 benchmark case.

(b) How sensitive are the simulated SBL characteristics to different SGS parameterizations when a hfbc is applied?

Turbulence smaller than the filter width Δ is represented in LESs by the SGS model. The SBL is characterized by weak turbulence in comparison to the convective boundary layer (Stull 1988). Consequently, the small intensity and size of turbulent eddies leads to a major impact of the SGS parametrization, which therefore significantly influences the shape of the mean wind and temperature profiles, especially close to the surface. As an example, idealized LESs by Peña et al. (2021) show that e_{SGS}/e (the ratio of SGS *TKE* to total *TKE*) of the SBL can be more than twice as large compared to convective or neutral cases near the surface. The impact of the SGS model can be reduced by decreasing the filter size Δ since smaller eddies can then be resolved directly. But even for SBL-LES with high resolution, the SGS model is still relevant. For instance, in simulations of Zhou and Chow (2011) with $\Delta x = 16$ m, $\Delta z = 5$ m and an applied surface heat flux of -20 mK m s $^{-1}$, e_{SGS} comprises 65 % of the total *TKE* when integrated over the simulation.

Almost all SGS models are purely dissipative, including the *TKE* closure model developed by Deardorff (1980) or modifications thereof (Sullivan et al. 1994). This is in accordance with Kolmogorov's theory of an inertial transfer regime where energy cascades from larger to smaller scales and then dissipates (see Pope (2000) for a detailed discussion about energy cascade theory). These approaches do not take into account nonlinear interactions of

small-scale turbulence with the mean flow leading to potential local backscattering of inertial energy from smaller to larger scales (Schumann 1995; Kosović 1997; Stoll et al. 2020). Regarding the SBL, where turbulence length scales are significantly smaller than in neutral or convective cases, it is beneficial to include nonlinear backscatter effects as they have been also observed and analyzed in measurements (Gucci et al. 2023).

This is incorporated in the Nonlinear Backscatter and Anisotropy (NBA) model by Kosović (1997): the parameterization for the SGS tensor includes nonlinear combinations of the strain rate tensor and the rotation rate tensor, allowing for energy transport from smaller to larger scales, i.e., energy backscatter. The intensity of energy backscatter is proportional to the so called backscatter parameter C_b (a detailed discussion of the NBA model is given in Sect. 2.3). By conducting parameter studies with different SGS models, we investigate the effect of the model change on the resulting vertical profiles and turbulence properties.

(c) How sensitive are the simulated SBL characteristics to the resolution of the numerical grid, when a hfbc is applied?

Grid sensitivity is the “lack of grid convergence" according to Maronga and Li (2021), i.e., LES results do not converge when decreasing the numerical grid size Δ. Ideally, results of LESs should be similar independent of grid size. However, in SBL-LESs, a decrease of boundary layer height with decreasing grid size was found in numerous studies (Beare et al. 2006; Sullivan et al. 2016; Maronga and Li 2021; McWilliams et al. 2023). Sullivan et al. (2016) describe this briefly in their simulations of GABLS1, where they show a decrease in boundary layer height for grid resolutions ranging from 2 m down to 0.39 m. Maronga and Li (2021) simulate the GABLS1 case with a crbc for grid sizes ranging from 12.5 m down to 1 m and observe no grid convergence. They show that high numerical dissipation correlates with grid spacing. Also the SGS model plays a role in their simulations except at very fine resolutions, where more turbulence is resolved in comparison to coarse resolutions. Maronga and Li (2021) also find that for a prescribed surface flux, grid sensitivity is slightly reduced down to $\Delta = 3.125$ m. The impact of grid sensitivity in combination with a hfbc is addressed as the last part of this work.

The outline of this paper is as follows: First, we present our methodology (numerical solver, governing equations, initial and boundary conditions of the moderately stable test case GABLS1) in Sect. 2. In Sect. 3 we establish our GABLS1 verification simulation and investigate how changes in the hfbc affect the results. This is followed by parameter studies with variations of the SGS model in Sect. 4 and variations of the grid size Δ in Sect. 5. Finally, a conclusion of the results and an outlook are given in Sect. 6.

2 Methodology

2.1 Governing Equations, EULAG and MPDATA

The numerical flow solver EULAG is applied in this work to solve the governing equations using MPDATA (multidimensional positive definite advection transport algorithm, Smolarkiewicz and Margolin 1998). In general, the approximation of the advection equation by an upstream scheme produces a second-order numerical error. With MPDATA, this error is not simply subtracted (unlike with other, classical finite-difference Lax-Wendroff schemes), but compensated by an additional upwind step with a pseudo-velocity (Smolarkiewicz and

Margolin 1998). MPDATA is therefore oscillation free and ideal for SBL simulations, as numerical errors are reduced to a minimum. EULAG works with an unstaggered Arakawa-A-grid, i.e., all variables are evaluated directly at their grid point. In our simulations, no explicit filter is applied and the numerical grid serves implicitly as the filter with grid size Δ.

The governing equations under Boussinesq assumption, including the Coriolis force for the resolved zonal, meridional and vertical velocity components $u_i, i \in \{1,2,3\}$ (u v and w) and the resolved potential temperature θ on a cartesian coordinate system, are (Prusa et al. 2008):

$$\frac{\partial u_i}{\partial x_i} = 0, \tag{1}$$

$$\begin{aligned} \frac{\mathrm{d}u_i}{\mathrm{d}t} = &- \frac{\partial(\pi - \pi_\mathrm{e})}{\partial x_i} && + f_\mathrm{c}\varepsilon_{ij3}(u_j - u_{\mathrm{e}j}) \\ &+ \delta_{i3} \cdot g\frac{(\theta - \theta_\mathrm{e})}{\theta_0} && - \alpha(u_i - u_{\mathrm{e}i}) && - \frac{\partial \tau_{ij}}{\partial x_j}, \end{aligned} \tag{2}$$

$$\frac{\partial(\theta - \theta_\mathrm{e})}{\partial t} = - u_i\frac{\partial \theta_\mathrm{e}}{\partial x_i} \quad - \alpha'(\theta - \theta_\mathrm{e}) \quad - \frac{\partial Q_i}{\partial x_i}, \tag{3}$$

where x_1, x_2, x_3 are to the x (stream-wise) and y (cross-stream) directions in the horizontal and z in the vertical, π the resolved density normalized pressure, $f_c = 2\Omega \sin\phi$ the Coriolis parameter (with earth's rotation rate Ω and ϕ the local latitude), $g = 9.81\mathrm{ms}^{-2}$ the acceleration due to gravity, θ_0 the potential temperature of a horizontally homogeneous hydrostatic reference state, and α, α' the relaxation coefficients. They are in general applied only near the upper boundary of the simulation to prevent oscillations. The subscript "e" refers to an environmental ambient state of the respective variable which is balanced by the Coriolis force, buoyancy and the pressure gradient force (Smolarkiewicz and Margolin 1997).

The effects of turbulent diffusivity on momentum and heat are parameterized via:

$$\tau_{ij} = \tau_{ij,\mathrm{S}} + \tau_{ij,\mathrm{SGS}}, \tag{4}$$

$$Q_i = Q_{i,\mathrm{S}} + Q_{i,\mathrm{SGS}}, \tag{5}$$

with the stress tensor τ_{ij} and the heat flux Q_i. Both are representing the sum of the surface boundary condition prescribed only on the lower surface boundary (see Sect. 2.2) and the SGS parameterization acting in the complete simulation domain including the surface (see Sect. 2.3).

2.2 Surface Boundary Condition for Heat and Momentum

Since EULAG uses a co-located Arakawa-A-grid, the surface fluxes $\tau_{ij,\mathrm{S}}$ and $Q_{i,\mathrm{S}}$ from Equations (4) and (5) are defined directly at the lower surface. For a flat, horizontal homogeneous lower surface, $Q_{i,\mathrm{S}} = \mathbf{1}_{\{z=0\ \mathrm{m}\}}(z)\delta_{i3}Q_\mathrm{S}$, i.e., we prescribe a vertical heat flux at $z = 0$ m. The prescribed heat flux will be characterized from now on as Q_S.

As all other models simulating the GABLS1 inter-comparison study apply a cooling rate at the surface, we aim to use Q_S to replicate a surface cooling linear with time for the purposes of comparison and validation. To achieve a surface temperature decreasing linearly with time, we impose a surface heat flux changing with the square root of the normalized time t/T, where t is the time variable in the simulation and T is the total simulated time:

$$Q_\mathrm{S} = A\sqrt{t/T}, \tag{6}$$

with a constant value A. This relationship can be derived as follows: the total accumulated cooling $\int \Delta\theta \, \mathrm{dz} = \Delta\theta_\mathrm{s} H_{\Delta\theta}$ is composed of the total surface temperature change $\Delta\theta_\mathrm{s}$ and the integral boundary layer depth $H_{\Delta\theta}$. The bulk turbulence scale $b = H_{\Delta\theta}/\Delta\theta_\mathrm{s}$ can be parameterized as $b \propto Q_\mathrm{S}^{-1}$ (Stull 1988). The total net heat flux Q_T is calculated as Stull (1988):

$$-\frac{\partial \Delta\theta_\mathrm{s} H_{\Delta\theta}}{\partial t} = -\frac{\partial \Delta\theta_\mathrm{s}^2 b}{\partial t} = Q_\mathrm{T}. \tag{7}$$

Identifying the total net heat flux Q_T with the surface heat flux Q_S, assuming a constant cooling rate $\Delta\theta_\mathrm{s} \propto t$ and using the proportionality of b leaves $\frac{\partial (t^2 Q_\mathrm{S}^{-1})}{\partial t} \propto Q_\mathrm{S}$. This is resolved by $Q_\mathrm{S} \propto \sqrt{t}$, as in Equation (6). For comparison, we also apply in Sect. 3 a constant heat flux:

$$Q_\mathrm{S} = B = \frac{2}{3}A, \tag{8}$$

where B is a constant value. The condition $B = \frac{2}{3}A$ ensures the same time-integrated surface heat flux regardless of the applied hfbc.

The surface stress is prescribed by an aerodynamic drag law using a constant drag coefficient (Epifanio 2007). More detailed information on the momentum boundary conditions of EULAG can be found in Prusa et al. (2008).

2.3 Description of the Implemented SGS Models

All SGS models we apply in this study are based on the *TKE* closure model: e (the *TKE*) is the sum of the resolved part e_res and the SGS part e_SGS. The latter is a priori unknown and parameterized via an additional equation, which can be solved along with the governing equations (1a-c) (Deardorff 1980; Sullivan et al. 1994):

$$\begin{aligned} \frac{\mathrm{d}e_\mathrm{SGS}}{\mathrm{d}t} &= \underbrace{-\tau_{ij,\mathrm{SGS}} S_{ij}}_{P} \underbrace{+\frac{g}{\theta_0} Q_{3,\mathrm{SGS}}}_{B} - \varepsilon + \underbrace{\frac{\partial \left(u_{i,\mathrm{SGS}}(e_\mathrm{SGS} + \pi_\mathrm{SGS})\right)}{\partial x_i}}_{D} \\ &=: fTKE. \end{aligned} \tag{9}$$

The right-hand side of Eq. (9), i.e., the sum of P, B, ε and D will be referred to as *fTKE* (forcings of the *TKE*). The first term P is the e_SGS production term with the resolved strain rate tensor $S_{ij} = \frac{1}{2}(\frac{\partial u_j}{\partial x_i} + \frac{\partial u_i}{\partial x_j})$. The second term B signifies the buoyancy production/destruction, ε is the viscous dissipation and term D denotes diffusion. Three different SGS

models are applied in this work: the Deardorff-Schumann (DES) closure and two modifications thereof, the Anisotropy (ANI) and the NBA model.

DES model

The DES parameterization of the SGS terms in Eq. (9) is Deardorff (1980):

$$\tau_{ij,\mathrm{SGS}} = -2K_\mathrm{m} S_{ij}, \tag{10}$$

$$Q_{i,\mathrm{SGS}} = -K_\mathrm{h} \frac{\partial(\theta - \theta_\mathrm{e})}{\partial x_i}, \tag{11}$$

$$(u_{i,\mathrm{SGS}}(e_\mathrm{SGS} + \pi_\mathrm{SGS})) = -2K_\mathrm{m} \frac{\partial e_\mathrm{SGS}}{\partial x_i}, \tag{12}$$

$$\varepsilon = c_\varepsilon e_\mathrm{SGS}^{3/2}/l, \tag{13}$$

with eddy viscosity $K_\mathrm{m} = c_\mathrm{m}\, l\sqrt{e_\mathrm{SGS}}$, $c_\mathrm{m} = 0.0856$, eddy diffusivity $K_\mathrm{h} = 0.204\, \frac{l\sqrt{e_{SGS}}}{1+0.3\Delta^2 N^2/e_{SGS}}$ (including the limitation of vertical scalar diffusion as suggested by Schumann 1991), $c_\varepsilon = 0.845$, $l = \min(\Delta, 0.845z)$ and N the Brunt-Väisälä frequency. In EULAG, Eq. (9) is modified to solve for $\sqrt{e_\mathrm{SGS}}$ instead of e_SGS. This approach is similar to Deardorff (1980), where also the modified equation can be found. All modifications for both the ANI and the NBA model to Eqs. (9) and (10) are explicitly stated below.

ANI model

The ANI model extends the DES model by taking into account the inhomogeneous flow characteristics in the z direction. The SGS stress tensor is modified according to Sullivan et al. (1994) to:

$$\tau_{ij,\mathrm{SGS}} = -2K_\mathrm{m}\gamma S_{ij} - 2(c_\mathrm{m} l)^2 \langle S\rangle \langle S_{ij}\rangle, \tag{14}$$

with $\gamma = \frac{S'}{S'+\langle S\rangle}$, $S' = \sqrt{2\langle (S_{ij} - \langle S_{ij}\rangle)(S_{ij} - \langle S_{ij}\rangle)\rangle}$ and $\langle S\rangle = \sqrt{2\langle S_{ij}\rangle\langle S_{ij}\rangle}$.

The values of K_m and c_m are identical to the DES model, i.e., the ANI model is also a *TKE*-based closure. When $\gamma = 1$ and $\langle S\rangle = 0$, $\tau_{ij,\mathrm{SGS}}$ becomes similar to the form in Equation (10).

NBA model

For the NBA model, the SGS tensor becomes, according to Kosović and Curry (2000):

$$\tau_{ij,\mathrm{SGS}} = -C_\mathrm{e}\Delta\left\{2\sqrt{e_\mathrm{SGS}}S_{ij} + \left(\frac{27}{8\pi}\right)^{1/3} C_\mathrm{s}^{2/3}\Delta\left[C_1\left(S_{ik}S_{kj} - \frac{1}{3}S_{mn}S_{nm}\delta_{ij}\right) + C_2\left(S_{ik}\Omega_{kj} - \Omega_{ik}S_{kj}\right)\right]\right\}, \tag{15}$$

with $C_\mathrm{e} = \left(\frac{8\pi}{27}\right)^{1/3} C_\mathrm{s}^{4/3}$, $C_\mathrm{s} = \left[\frac{8(1+C_\mathrm{b})}{27\pi^2}\right]^{1/2}$, $C_1 = C_2 = \frac{960^{1/2}C_\mathrm{b}}{3.5(1+C_\mathrm{b})}$ and the rotation rate tensor $\Omega_{ij} = \frac{1}{2}(\frac{\partial u_j}{\partial x_i} - \frac{\partial u_i}{\partial x_j})$. The backscatter parameter is $C_\mathrm{b} = 0.36$. Notice that if $C_\mathrm{b} = 0 \Rightarrow C_1 = C_2 = 0$ and $\tau_{ij,\mathrm{SGS}}$ becomes similar to the form in Equation (10). The resulting SGS production term P from Equation (9) of the NBA model is according to Kosović (1997):

$$P = -\tau_{ij,\mathrm{SGS}} S_{ij} = \underbrace{C_\mathrm{e} \Delta \sqrt{e_\mathrm{SGS}} 2 S_{ij} S_{ij}}_{\text{linear}} + \underbrace{\left(\frac{27}{8\pi}\right)^{1/3} C_\mathrm{s}^{2/3} C_\mathrm{e} \Delta^2 C_1 S_{ik} S_{kj} S_{ij}}_{\text{nonlinear}}, \tag{16}$$

being the sum of a linear and a nonlinear contribution. The isotropic contribution and the terms including rotation rate tensors from Equation (15) become zero when being multiplied with S_{ij} and are therefore not present in Eq. (16).

2.4 Simulation Setup

Following the GABLS1 setup, the test-case boundary conditions are based on the Beaufort Sea Arctic Stratus Experiment (BASE) dataset of flight measurements in the Arctic, details can be found in Beare et al. (2006) and Kosović and Curry (2000). In the simulation setup, the domain size is $(400\ \mathrm{m})^3$ with periodic lateral boundary conditions. We apply a uniform grid size $\Delta \in \{12.5, 6.25, 3.125, 2\}$ m. For the majority of the simulations discussed below, a grid size of 6.25 m was applied. This resolution is motivated by the profiles with $\Delta = 6.25$ m of the inter-comparison benchmark of GABLS1 (Beare et al. 2006), which are used for validation. In addition, $\Delta = 6.25$ m ensures a significant contribution of the SGS-model and reasonable computational time and costs in comparison to more fine-scaled simulations. The air density is $\rho_0 = 1.3223\ \mathrm{kg\ m^{-3}}$. The SBL is driven by a geostrophic wind of $u_\mathrm{g} = u_\mathrm{e} = 8\ \mathrm{m\ s^{-1}}$ in the zonal direction. Its meridional component is $v_\mathrm{g} = v_\mathrm{e} = 0\ \mathrm{m\ s^{-1}}$. The resolved velocities are set to zero at the lowest grid point in the vertical (no-slip boundary condition) and a bulk aerodynamic drag coefficient of $c_\mathrm{D} = 0.03$ is used. This value was inferred from other GABLS1 participants and EULAG MOST simulations, and adopted for the here applied no-slip condition at the surface. The initial and environmental temperature profile θ_e remains neutral ($\theta_0 = 265$ K) up to $z = 100$ m, with an inversion above characterized by a lapse rate of $0.01\ \mathrm{K\ m^{-1}}$. Similar to Sullivan et al. (2016), $e_\mathrm{SGS}(t = 0) = 0.4(1 - z/250\ \mathrm{m})^3 \mathrm{m^2 s^{-2}}$ for $z < 250$ m to initiate turbulence, and 0 above. The simulated time period is 9 h following Beare et al. (2006).

In literature, simulations of GABLS1 are conducted with a cooling rate of $0.25\ \mathrm{K\ h^{-1}}$ at the lower surface boundary. In contrast to this approach, we will apply a surface heat flux with two options: A negative surface heat flux proportional to $\sqrt{t/T}$ or a constant value (see Sect. 2.2 and Table 1), depending on the respective simulation. The latitude is $\phi = 73°$, corresponding to a Coriolis parameter of $f_c = 1.39 \times 10^{-4} \mathrm{s^{-1}}$ We omit the constant flux layer approach, which is commonly used in most other LES models due to the reasons described above. An EULAG control simulation of GABLS1, with a constant flux layer and an applied surface cooling rate, is discussed in detail in Englberger et al. (2026). The top boundary is represented by an impermeable lid ($w = 0$) with a free-slip boundary condition for u and v, and we impose a 100 m thick sponge layer with damping coefficients $\alpha = \alpha' = 0.04\ \mathrm{s^{-1}} \cdot H(z - 300\mathrm{m})$ (with H the Heaviside step function) to attenuate oscillations. All simulations are listed in Table 1.

2.5 Evaluation of Simulation Results

We calculated horizontally-averaged mean vertical profiles over the last simulation hour (indicated by $\langle ... \rangle$), similar to Beare et al. (2006) and Kosović and Curry (2000), for the

Table 1 All simulations of this study, discussed in the respective sections. Grid spacing is always identical in x, y and z directions

Section	Name	$Q_S(t)$ (−mK m s^{-1})	SGS model	Grid spacing Δ (m)
Section 3	G06250	$12.5\sqrt{t/T}$	NBA	6.25
	G06250c	$\frac{2}{3}12.5 = 8.33$	NBA	6.25
Section 4	G06250	$12.5\sqrt{t/T}$	NBA	6.25
	G06250c	$\frac{2}{3}12.5 = 8.33$	NBA	6.25
	G06250a1	$12.5\sqrt{t/T}$	ANI	6.25
	G06250a	$8.5\sqrt{t/T}$	ANI	6.25
	G06250ac	$\frac{2}{3}8.5 = 5.66$	ANI	6.25
	G06250d1	$12.5\sqrt{t/T}$	DES	6.25
	G06250d	$7.5\sqrt{t/T}$	DES	6.25
	G06250dc	$\frac{2}{3}7.5 = 5$	DES	6.25
Section 5	G12500	$12.5\sqrt{t/T}$	NBA	12.5
	G06250	$12.5\sqrt{t/T}$	NBA	6.25
	G03125	$12.5\sqrt{t/T}$	NBA	3.125
	G02000	$12.5\sqrt{t/T}$	NBA	2
	G12500a	$8.5\sqrt{t/T}$	ANI	12.5
	G06250a	$8.5\sqrt{t/T}$	ANI	6.25
	G03125a	$8.5\sqrt{t/T}$	ANI	3.125
	G02000a	$8.5\sqrt{t/T}$	ANI	2
	G02000d	$7.5\sqrt{t/T}$	DES	2
App	G02000	$12.5\sqrt{t/T}$	NBA	2

resolved wind speed components and the resolved potential temperature. For the turbulence analysis in Sect. 3, we utilize the gradient Richardson number (Stull 1988):

$$Ri = \frac{\frac{g}{\theta}\frac{\partial\theta}{\partial z}}{\frac{\partial u}{\partial z}^2 + \frac{\partial v}{\partial z}^2}. \tag{17}$$

Commonly, $Ri < Ri_c$ (where Ri_c about 0.2−0.25 is the critical Richardson number) is considered as necessary (but not sufficient) criterion for sustained turbulence (Stull 1988). Although studies of *Ri* by Galperin et al. (2007) have questioned the use of Ri_c in the SBL (as turbulence can survive for values of $Ri \gg 0.25$), Grachev et al. (2012) and Mahrt (2014) indicate that Ri_c can be used to distinguish between the vSBL and the wSBL regime. In addition, Grachev et al. (2012) defines within the wSBL the regime where $Ri < 0.1$ as surface-layer regime.

Resolved fluctuations are $u_i - \langle u_i \rangle_{xy}$ relative to the horizontal mean. SGS stresses $\tau_{ij,\mathrm{SGS}}$ are calculated via the eddy viscosity relation, the SGS vertical heat flux via the eddy diffusivity relation given in Equations (10) and (11). The SGS *TKE* e_{SGS} is obtained as a variable from the simulations. The total stresses $u_i'u_j'$ and e (the total *TKE*), are given as a summation of the resolved fluctuations and the SGS stresses. The properties

mentioned above for stresses also apply to the vertical heat flux: the total turbulent heat flux $w'\theta'$ is the sum of the resolved component and Q_3. The friction velocity is calculated via $u_*^2 = (\langle u'w' \rangle^2 + \langle v'w' \rangle^2)^{1/2}|_{z=0\ \mathrm{m}}$ (i.e., including SGS stresses). u_* and $\theta_* = \langle w'\theta' \rangle u_*^{-1}|_{z=0\ \mathrm{m}}$ are used in Sect. 4 for normalization of vertical profiles.

3 Variation of the Surface Heat Flux Condition

In this section, we validate our setup of EULAG with the NBA SGS model and a time-dependent hfbc against the GABLS1 benchmark case. The unsuitability of a constant surface heat flux for the validation of GABLS1 is also demonstrated. We thus address here question (a) from Sect. 1: what effect do the different types of hfbcs have on imulation results of a weakly SBL?

For reasons of comparability with other GABLS1 studies, we aim for an approximately linear cooling of the surface with time by imposing a surface heat flux of $Q_\mathrm{S} = -12.5\sqrt{t/T}\ \mathrm{mK\ m\ s^{-1}}$ (with $A = -12.5\ \mathrm{mK\ m\ s^{-1}}$, see Eq. 6). The value of the coefficient A was estimated by conducting simulations with various coefficient values and choosing the one where a final surface cooling of ≈ 2.25 K is achieved after nine hours, as in Beare et al. (2006). Because this simulation is performed with a resolution of $\Delta = 6.25$ m, it is referred to as G06250 hereafter. It is compared to a simulation, where the imposed surface heat flux is constant ($B = -8.33\ \mathrm{mK\ m\ s^{-1}}$, see Eq. 8) with time, subsequently referred to as G06250c. The value of $B = 2/3A$ is identical to the temporal mean of the prescribed surface heat flux in G06250. For both G06250 and G06250c, the NBA SGS model (see Sect. 2.3) is applied, similar to Kosović and Curry (2000). We will justify the choice of this SGS model with a heat flux surface boundary condition below in sensitivity studies in Sects. 4 and 5. The panels in Fig. 1 display the hourly evolutions of the resulting vertical wind speed ($u_\mathrm{h} = \sqrt{u^2 + v^2}$) (Fig. 1a, d) and θ profiles (Fig. 1b, e). We are specifically interested in the difference between G06250 and G06250c (Fig. 1g, h) and its explanation.

The wind speed profile (Fig. 1a) of the final hour of G06250 has a significant overlap with the range of simulations from Beare et al. (2006) (gray area). The maximum wind speed height (i.e., the LLJ position) is at $z \approx 170$ m and the change of u_h with height is in agreement with Beare et al. (2006). Also the potential temperature profile (Fig. 1b) lies within the range of GABLS1. We observe cooling over all heights similar to the reference simulations, and a temperature inversion below the LLJ at $z \approx 150$ m. The Reynolds stresses and the turbulent heat flux will be discussed in Sect. 4. The temporal evolution of the G06250c profiles differs significantly. For u_h (Fig. 1d), in contrast to G06250, the magnitude of the LLJ is significantly larger in the middle time period of the simulation compared to the ending time and compared to G06250 (see Fig. 1c). The final, less pronounced wind speed maximum exhibits strongly reduced overlap with the inter-comparison simulations from Beare et al. (2006). For the potential temperature in Fig. 1e, in the initial simulation hours, strong cooling occurs only close to the surface up to $z \approx 100$ m. During later hours ($t > 5$ h), the surface temperature negligibly changes with time while the inversion layer grows.

The change in wind direction with time and height is displayed in the hodographs (Fig. 1c, f). The Ekman spiral of G06250 is similar in shape and magnitude of (u, v) to the one after 12 h of simulation in Kosović and Curry (2000) (Fig. 17). Regarding G06250c, v decays significantly in intensity after reaching its maximum value and the resulting Ekman

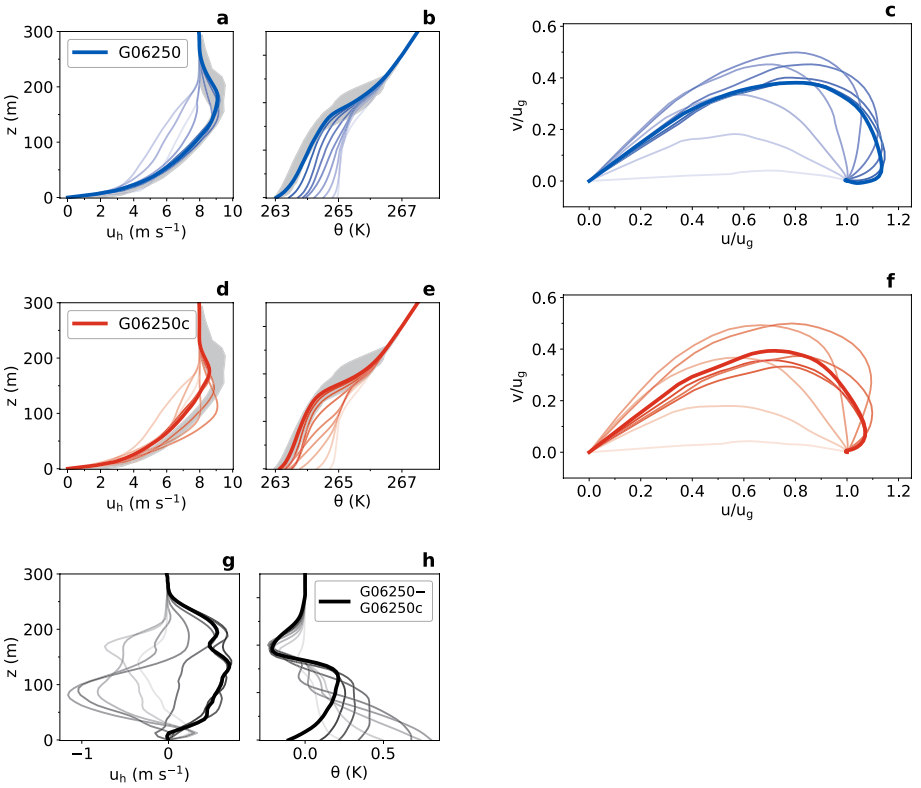

Fig. 1 Simulation results of G06250 and G06250c, see Table 1. (**a**, **b**, **d**, **e**) : final vertical profiles of u_{h} and potential temperature θ (thick colored lines). Hourly profiles are shown by transparent lines, progressing from lighter to darker. The shaded gray area defines the range of profiles of published simulations with the same resolution from Beare et al. (2006) (**c**, **f**): normalized hodographs of G06250 and G06250c. (**g**, **h**): difference of the vertical profiles

spiral is more skewed than for G06250. The contrast in the temporal evolution of both simulations is visible in Figs. 1g and h: for intermediate times, the difference of u_{h} is strongly negative (> -1 m s^{-1}) around $z \approx 100$ m, as a short-term, strong LLJ forms in G06250c. The intermediate positive values of the θ-difference indicate that initial surface cooling is stronger in G06250c.

What exactly leads to the differences in LLJ characteristics (i.e., height, intensity) and the evolution of the potential temperature between the profiles of G06250 and G06250c in Fig. 1? The only difference in the simulation setup is the surface hfbc, potentially influencing the turbulent heat flux in the layers above. This might alter the balance of buoyancy versus shear and ultimately affect the mean wind speed and potential temperature. To examine the turbulence dynamics in greater detail, time-height cross-sections of the following horizontally-averaged variables are analyzed: the horizontal wind speed (Fig. 2a, b), the turbulent heat flux (Fig. 2c, d) and the gradient Richardson number (Fig. 2e, f). Figure 2g and h show the temporal evolution of the horizontally-averaged potential temperature at different heights z up to $z = 100$ m.

To address the question posed above, we begin by focusing on simulation G06250c (right column in Fig. 2). Regarding the wind speed, the maximum height of the 9 m s^{-1} isoline for G06250c in Fig. 2b is smaller than in Fig. 2a for G06250, indicating that the boundary layer height is reduced for the case with a constant applied surface heat flux. In addition, the final LLJ intensity of G06250c is weakened relative to G06250, the maximum wind speed appears only between $t = 4$ h and $t = 5$ h.

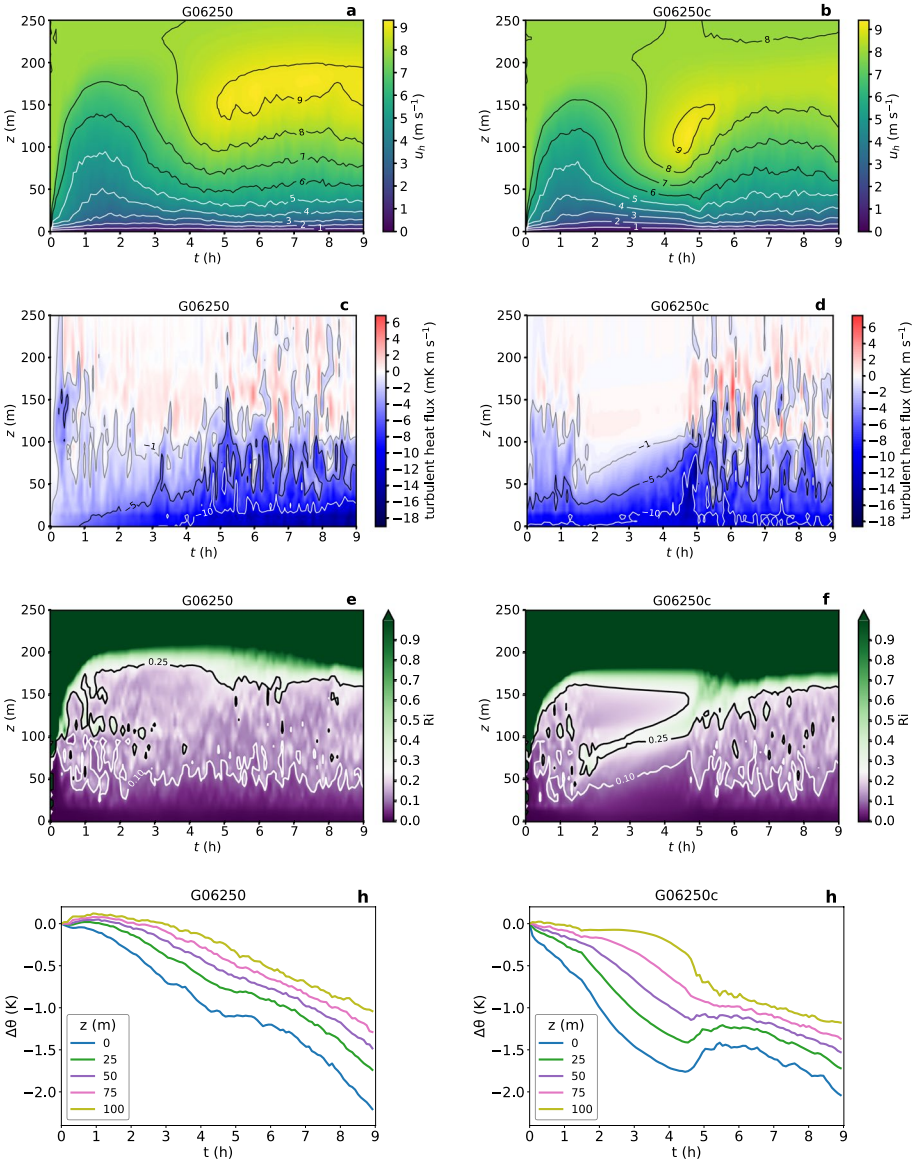

Fig. 2 Illustration of the temporal evolution of horizontally-averaged variables for simulations G06250 and G06250c. (**a**, **b**): u_h plotted over time and height. (**c**, **d**): turbulent heat flux intensity plotted over time and height, black isoline: -5, white isoline: -10 mK m s^{-1}. (**e**, **f**): gradient Richardson number *Ri* plotted over time and height (**g**, **h**):potential temperature for different heights plotted versus time

We observe an intense turbulent heat flux close to the surface (< -10 mK m s^{-1}) in Fig. 2d throughout the simulated time, in combination with a rapid decrease in magnitude with height between $t = 2$ h and $t \approx 5$ h (10 mK m s^{-1} over the lowest 100 m). Additionally, the isolines of -5 and -1 mK m s^{-1} increase gradually in height over this time period. Correspondingly, in Fig. 2f, a thin layer of $Ri > 0.25$ emerges between $z \approx 50$ m and $z \approx 100$ m in the interval of $t \approx 2 - 5$ h and increases over time with height. The intense heat flux close to the surface leads to a decoupling of the temperature, presented in Fig. 2f: strong cooling close to the surface ($z = 0$ m and $z = 25$ m) and almost no cooling higher up ($z = 100$ m) until $t = 5$ h. The intense surface cooling ultimately results in a shallow, strongly stratified surface layer between $t = 4$ h and $t = 5$ h (Fig. 2b, d) and an associated decrease of turbulent stress and turbulent heat flux. This leads to an imbalance with the now dominating Coriolis force and the LLJ evolution with wind speeds above 9 m s^{-1} (Fig. 2b), which is in line with the theory developed by Shapiro and Fedorovich (2010).

Later, at around 5 h, a "shock" is visible in the images of G06250c (Fig. 2, right column): the wind speed around $z = 100$ m gets reduced (the isolines increase in height, Fig. 2b), an instantaneous burst of turbulent heat flux arises (Fig. 2d) and the temperature up to $z = 50$ m suddenly increases while it sharply decreases at $z = 100$ m (Fig. 2h). We hypothesize that the large shear built up by the LLJ leads to a Kelvin-Helmholtz instability, where the super-geostrophic wind speed triggers the sudden generation of turbulence. This can be further understood by analyzing *Ri* (see Sect. 2.5) in Fig. 2c: for $t = 2 - 5$ h, the layer of $Ri > 0.25$ around $z \approx 100$ m indicates a vSBL with weak turbulence. The shear below increases over time (visible by the rise of the isolines) and the layer of $Ri > 0.25$ rises, which ultimately is followed by the turbulent burst between $t = 4 - 5$ h.

This process could be interpreted as a "regime change" of a vSBL to a wSBL regime. According to Sun et al. (2012), a threshold velocity separates these two regimes. The LLJ might serve as trigger as it causes this excession past the threshold velocity and ultimately the change of a strongly to a weakly SBL. The end result after 9 h is a reduction in the LLJ intensity (observable in Fig. 1b), a continuous turbulent heat flux up to 200 m (Fig. 2d), a value of $Ri < 0.25$ throughout the boundary layer (Fig. 2f) and a similar cooling at different height levels (Fig. 2h).

Regarding the G06250 simulation, no continuous layer of $Ri > 0.25$ forms around $z = 100$ m (Fig. 2e). The surface heat flux at the beginning of the simulation is, by design, smaller in magnitude compared to G06250c (Fig. 2c), and therefore the surface cooling is much less intense in the first hours (Fig. 2g). The temperature in the layers above increases with time at the very beginning, since initially triggered turbulence leads to downward transport of warmer air from the upper layers with no counter-transport of colder air from below. At $t \approx 5$ h (the onset of the LLJ), the temperature at the surface and at $z = 25$ m stay constant over a short time. After this plateau, they decrease again. The turbulent heat flux (Fig. 2c) does not suddenly "burst" at 5 h for G06250, as is the case in G06250c, but rather transitions smoothly to a different turbulence regime with more intense turbulent heat fluxes above $z = 100$ m. The LLJ emerging between 4 and 5 h (Fig. 2a) does not partially break down as for G06250c and the horizontal wind converges to an equilibrium state. The *Ri*-isoline of 0.25 visible in Fig. 2e decreases as the LLJ emerges. In conclusion, we find that the application of a surface heat flux decreasing with time (G06250) ensures continuous turbulence as it both avoids runaway cooling and a decoupling of the surface temperature.

4 Variation of the Subgrid Scale Model

In the following section, research question (b) from Sect. 1 is addressed: how sensitive are the simulated SBL characteristics to different SGS parameterizations when a hfbc is applied? This is investigated by setting all simulation parameters identical to G06250 and varying only the SGS model (see Table 1).

4.1 Impact on First- and Second-Order Statistics

For all three SGS models with the same applied surface heat flux of $Q_S = -12.5\sqrt{t/T}$ mK m s^{-1}, Fig. 3 shows the vertical profiles for various mean variables and Fig. 4 for various turbulent variables. Turbulent fluxes are normalized with respect to u_*^2 or θ_* (see Sect. 2.5).

In the vertical profiles of the total and meridional wind speed (Fig. 3a, b), the DES and ANI SGS models exhibit a diminished boundary-layer height (encompassing a lower altitude of the LLJ). Regarding the horizontal wind speed, only the profile of the NBA model has a significant overlap with the results of the GABLS1 inter-comparison from Beare et al. (2006) (indicated here in gray), as discussed in detail in Sect. 3. For the meridional wind speed v, the qualitative trend with increasing z is similar for all three models: an increase up to a maximum of ≈ 3 m s^{-1} followed by a decrease and a minimum < 0 m s^{-1} and then a return to 0 m s^{-1}. Regarding the potential temperature profiles in Fig. 3c, only for the NBA model (G06250) substantial cooling up to 200 m and a result similar to Beare et al. (2006) is achieved. The final surface temperature is ≈ 2 K warmer for the NBA model in contrast to the other two models. The hodographs in Fig. 3d of all three simulations are similar in shape, but the markers indicate the differences in boundary layer height, as evident by the different wind speed components for the circular marker at $z = 100$ m.

The shape of the mean profiles in Fig. 3 can be interpreted by analysis of the turbulent heat flux and Reynolds stresses displayed in Fig. 4. The normalized vertical turbulent heat flux in Fig. 4a describes the magnitude of upward (downward) transport of cold (warm) air when the sign is positive. Only the NBA model displays significant resolved fluxes up to $z = 100$ m. As a result, more cool air is transported upwards which leads to a significant decrease of potential temperature throughout the boundary layer, visible in Fig. 3c.

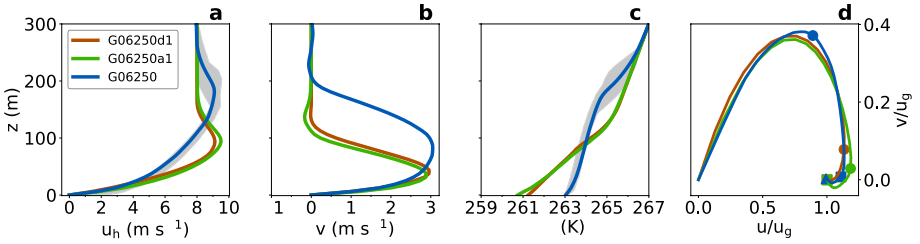

Fig. 3 Mean variable profiles of simulations with identical surface heat flux and different SGS models: the DES model (G06250d1), the ANI model (G06250a1) and the NBA model (G06250): (**a**) horizontal wind, (**b**) meridonal wind component, (**c**) potential temperature, (**d**) hodograph with circle ($z = 100$ m), square ($z = 200$ m) and triangle marker ($z = 300$ m). All profiles are averaged over the horizontal plane and the last simulation hour. Gray shading as in Fig. 1

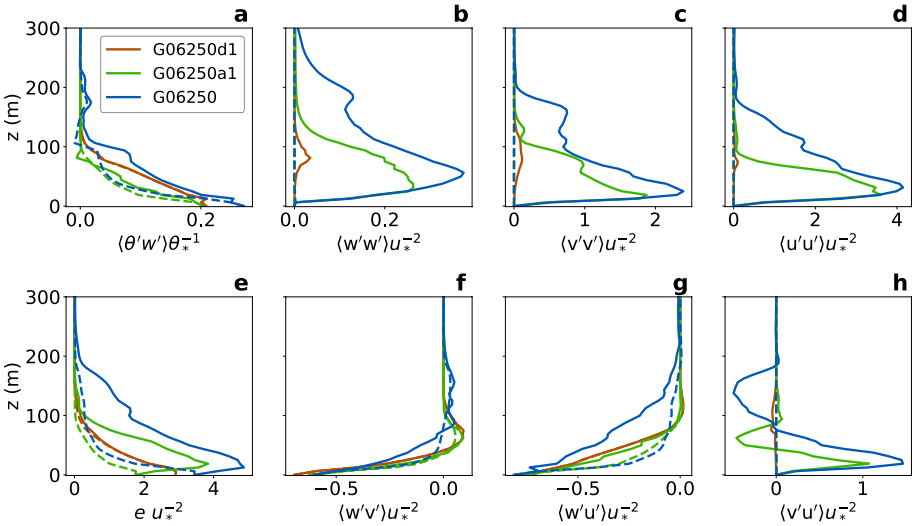

Fig. 4 Turbulent variable profiles of simulations with varying SGS model and identical surface heat flux: (**a**) vertical turbulent heat flux, (**b**–**d**) diagonal Reynold stresses, (**e**) *TKE* and (**f**–**h**) off-diagonal Reynold stresses. All profiles are averaged over the horizontal plane and the last simulation hour. Dashed lines indicate SGS contributions, solid lines indicate the total (SGS + resolved) contribution

Next, the variances ($\langle w'w'\rangle$, $\langle v'v'\rangle$, $\langle u'u'\rangle$, Fig. 4b-d) are analyzed. The SGS stresses become 0, since $S_{ii} = 0$ (Eq. 1a). The resolved variances of the NBA model are the largest with a significant contribution of $\langle v'v'\rangle$ and $\langle u'u'\rangle$ up to 200 m and a contribution of $\langle w'w'\rangle$ even up to 300 m. This is reflected in the mean wind speed profiles, as a return to geostrophic wind occurs at a higher altitude than for the other simulations (Fig. 3a-b). The profiles of the DES model show a maximum at $\approx$ 80 m and are the smallest in magnitude compared to the other simulations. Even though the mean wind speed profiles in Fig. 3 of the simulation with the ANI model (G06250a1) are similar to the DES model simulation G06250d1, the variances are substantially larger. This is an indicator that the flow of G06250a1 is not fully laminar as in G06250d1 and that we observe some resolved turbulence. Similar characteristics as for the variances hold for the total (i.e., resolved + SGS) *TKE* (Fig. 4e): the smallest values occur for the DES model with no resolved *TKE* (overlap of SGS and total contribution), with larger values for the ANI model and the largest values over all heights for the NBA model. The total *TKE* of the NBA model is comparable to the results of Sullivan et al. (2016)(Fig. 7) considering magnitude and vertical gradient.

Lastly, we analyze the momentum fluxes ($\langle w'v'\rangle$, $\langle w'u'\rangle$, $\langle v'u'\rangle$, Fig. 4f–h). The profiles for the ANI and the NBA models follow qualitatively the typical characteristic curves for the covariances of the SBL (e.g., Sullivan et al. (2016) (Fig. 6) and Kosović and Curry (2000) (Fig. 9)): $\langle w'v'\rangle$ and $\langle v'u'\rangle$ exhibit a change of sign at the height of the v maximum and $\langle w'u'\rangle$ increases with increasing height and tends to zero some meters above the maximum of the total wind speed. The magnitude of the covariances is larger for the NBA model compared to the ANI model and the profiles additionally reach higher up in the vertical (i.e., characteristic maxima and zero-crossings appear for larger z). The profiles of the DES model (G06250d1) exhibit approximately the same shape as G06250a1 for w' covariances. The $\langle v'u'\rangle$-profile is close to zero, i.e., vertical turbulence is neither resolved nor parameter-

ized. In summary, the simulation with the NBA SGS model shows the stress tensor with the largest intensity achieving significant turbulence at higher altitudes in comparison to the other two SGS models.

4.2 Interpretation of the SGS Model Impact

How can we explain the differences in the vertical profiles of different SGS models in Figs. 3 and 4? To answer this and also the second research question posed in this work, we analyze *fTKE*, i.e., the right hand side of the e_{SGS} equation (Eq. 9) as it encapsulates production and dissipation of e_{SGS}. The *fTKE* averaged over the whole domain plotted versus time is shown in Fig. 5a. The resulting temporal evolution of the total *TKE* is shown in Fig. 5b.

We will first focus on the results from the NBA model, G06250. *fTKE* is largest compared to the other models, with a global maximum shortly after the beginning of the simulation and a second, local maximum around $t = 6\mathrm{h}$. In the spin-up phase (i.e., for $t < 1$ h), a significant partition of *fTKE* stems from the nonlinear part of the e_{SGS} production term defined in Eq. (16). Presumably, the nonlinear contribution is the main driver of continuous turbulence in the beginning of the simulation, as it leads to an increase in e_{SGS}, which vice versa increases the linear production term as it depends on $\sqrt{e_{\mathrm{SGS}}}$ (see Eq. 16). The first maximum in *fTKE* and *TKE* arises from the initial shear caused from the initial wind speed profiles. The second maximum can be explained with the onset of the LLJ between 4 h and 5 h (see Fig. 2a). The temporal evolution in *TKE* up to the simulated 9 h is in line with the observations from Maronga and Li (2021) (Fig. 2), who simulated the GABLS1 case with a duration of 36 h. We also extended our simulation time to 36 h for G06250, which does not have a relevant impact on the main findings of this work and therefore we limit the simulations to 9 h similar to Beare et al. (2006).

The other two models (DES G06250d1 and ANI G06250a1) show a completely different picture. At the start of the simulated time period, $fTKE < 0$. This can be interpreted as a dissipation of e_{SGS}. For the ANI model in Fig. 5a, we see *fTKE* fluctuations around 0 evolving shortly before $t = 1$ h with a global maximum at $t \approx 1$ h. Correspondingly, the *TKE* of G06250a1 shows a global maximum shortly after 1 h with following fluctuations (Fig. 5b). For the DES model, the *fTKE* is equal to zero after the initial dissipation phase, resulting in an initial dissipation of *TKE* in the first hour and a small *TKE* of $\approx 0.02\ \mathrm{m^{-2}s^{-2}}$ which is then constant with time. The investigated behavior of *TKE* and *fTKE* therefore closely

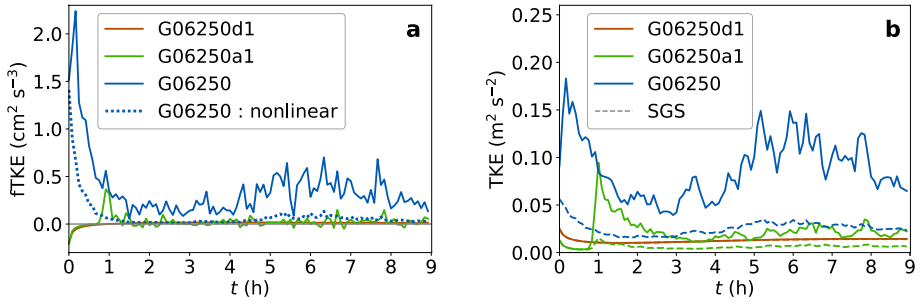

Fig. 5 (**a**) Solid lines: Domain-averaged *fTKE* plotted over time. Dotted line: contribution of nonlinear part in the NBA model according to Eq. (16). (**b**): Domain-averaged *TKE* over time including SGS part (dashed lines) and total *TKE* (solid lines) for the simulations with the same boundary conditions except for the SGS model (G06250: NBA, G06250a1: ANI, G06250d1: DES)

coincide with the differences in the vertical profiles of the NBA model in comparison to the other two models in Figs. 3 and 4.

4.3 Adaptation of Surface Heat Flux with Regard to the SGS Model

Up to now, the same surface heat flux of $-12.5\ \sqrt{t/T}$ mK m s^{-1} was applied as a lower surface boundary condition for all simulations with varying surface heat flux (i.e., G06250, G06250d1 and G06250a1). The final surface temperature differs significantly (≈ 2 K, Fig. 3c) between the models, as upward turbulent transport of cold air is reduced for the ANI and the DES model. To achieve better comparability of the potential temperature with published results from Beare et al. (2006) (Fig. 2 and 3), the magnitude of the surface heat flux for G06250a1 and G06250d1 will be adapted such that a similar final surface temperature is achieved. For the ANI model, this requires a surface heat flux of $-8.5\ \sqrt{t/T}$ mK m s^{-1} (G06250a). For the DES model, a value of $-7.5\sqrt{t/T}$ mK m s^{-1} (G06250d) is applied (see Table 1). In addition, we want to investigate how the resulting profiles of the ANI and the DES model simulations change when we apply a constant heat flux (simulations G06250ac and G06250dc).

The final vertical wind speed and potential temperature profiles are shown in Fig. 6a and b. Dash-dotted lines represent cases with a constant surface heat flux over time. Only the profiles corresponding to G06250 agree with the range of profiles from Beare et al. (2006) (grey shaded area). The differences between G06250 and G06250c have been discussed in Sect. 3. In comparison to the simulation performed with the NBA model, we observe major differences with the ANI and the DES model: the LLJ height in Fig. 6a is larger as the surface heat flux magnitude is smaller compared to G06250a1 and G06250d1 shown in Fig. 3a. The θ profiles in Fig. 6b differ in shape compared to Fig. 3c, as substantial cooling reaches a higher altitude. Regarding the *TKE* profiles in Fig. 6c, the NBA model yields the largest *TKE* for both a constant and a varying surface heat flux, followed by the ANI model. We will show below in Sect. 5.2 and Fig. 8 that the difference between the ANI and the NBA model stems from less intense large-scale *TKE* in the ANI model. For all models, e_{SGS} is similar regardless of the surface boundary condition. The DES model yields no resolved turbulence.

Figure 6d summarizes the effect of different heat fluxes and SGS models on the temporal evolution of the surface potential temperature. When a constant heat flux is applied (dash-dotted lines), the surface potential temperature decreases faster for all models at the beginning than at the end of the simulation. When the heat flux increases in magnitude proportional to $\sqrt{t/T}$ (solid lines), the potential temperature decrease is approximately linear, with fluctuations caused by resolved turbulence. The final surface potential temperature is smaller than for the corresponding constant hfbc simulations, even though the integrated surface heat flux over the simulated time period is identical in both cases.

Even when adapting the closure constant c_{m} of the DES and the ANI model to the value C_{e} of the NBA model (not shown), none of these simulations lead to results comparable to GABLS1 in terms of height and intensity of the LLJ and the temperature inversion. Only EULAG simulations with the NBA model and a variable surface heat flux result in final profiles comparable to Beare et al. (2006), so we will focus on this setup in the following section.

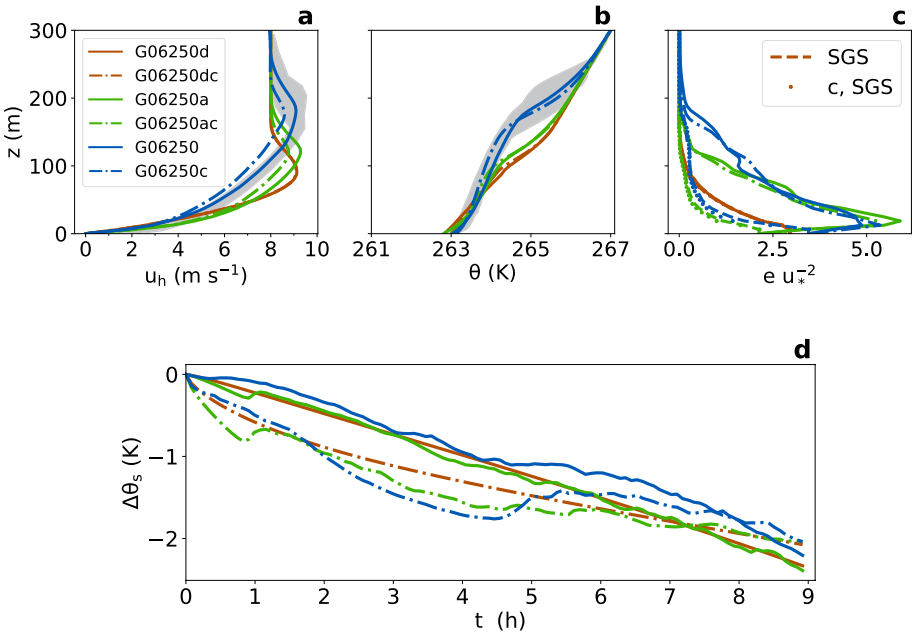

Fig. 6 (**a**) Horizontal wind, (**b**) potential temperature and (**c**) *TKE* profiles of simulations with constant ("...c") and varying surface heat flux for different SGS models (see Table 1). (**d**) Difference of surface temperature to initial surface temperature $\Delta\theta$ plotted over time. Dash-dotted lines indicate simulations with a constant surface heat flux, dashed lines e_{SGS} of simulations with varying surface heat flux and dotted lines e_{SGS} of simulations with constant surface heat flux. Gray shading as in Fig. 1

5 Investigation of the Grid Sensitivity

5.1 Impact on First- and Second-Order Statistics

The aim of this section is to answer question (c) from Sect. 1, i.e., analyze the grid sensitivity of the EULAG simulations and the effect of grid size variation on the final vertical profiles. This investigation is relevant, as a general finding for SBL simulations is a reduction of boundary-layer height with decreasing grid size (Maronga and Li 2021). Therefore, we conduct simulations with the NBA model and a time-varying surface hfbc for grid sizes Δ of 12.5 m, 6.25 m, 3.125 m and 2 m (see Table 1). We validated the simulation with $\Delta = 2$ m against the corresponding simulations in Beare et al. (2006) and also characterized the resolved small-scale turbulent eddies and temperature fronts (see Appendix). The resulting vertical profiles of total wind speed, potential temperature and *TKE* (SGS and total) are displayed in Fig. 7.

The LLJ height in the wind speed profiles (Fig. 7a) decreases with decreasing grid size. This behavior is in accordance with the findings of the inter-comparison study by Beare et al. (2006). Additionally, the LLJ height of all four profiles is also comparable to the 6.25 m-profiles of the inter-comparison (indicated by the gray shaded area). Consistent with the behavior observed in the wind speed profiles, the potential temperature profiles in Fig. 7b also show a decrease of the boundary layer height for decreasing Δ, accompanied by a decrease in final surface temperature.

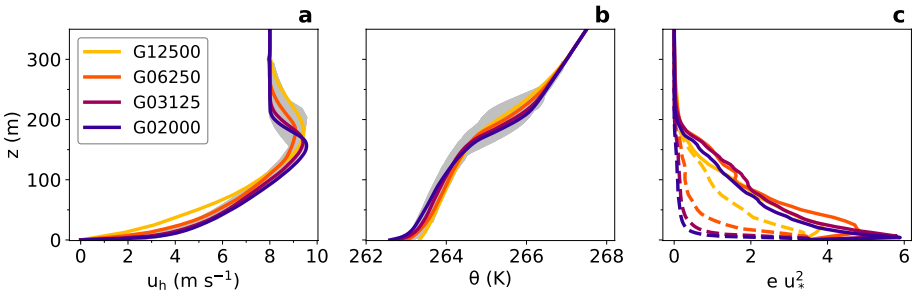

Fig. 7 (**a**) Horizontal wind, (**b**) potential temperature and (**c**) normalized *TKE* profiles (dashed lines represent e_{SGS}) of simulations with different resolutions (see Table 1). Gray shading as in Fig. 1

Table 2 Ratio of e_{sgs}/e (averaged over the final simulation hour and over the simulation domain) for the simulations with the NBA SGS model

Simulation	G12500	G0650	G0650c	G03125	G02000
Δ	12.5	6.25	6.25	3.125	2
e_{sgs}/e [%]	71.8	31.3	29.2	16.3	12.3

All total *TKE* profiles (solid lines in Fig. 7c) indicate resolved turbulence up to $z \approx 200$ m. The e_{SGS} (dashed lines in Fig. 7c) decreases with decreasing grid size over all heights. Table 2 shows that this decrease also applies to the domain-wide integrated fraction e_{SGS}/e. This behavior is expected, as the unresolved eddies become smaller and less intense for a smaller grid size and thus contain less *TKE*. We see this also in the equation for the SGS parameterization (Eq. 15). At the same time, the resolved *TKE* increases with decreasing grid size close to the surface. This can be explained by the reduction of the vertical turbulent length scale when approaching the lower boundary. With finer grid size, more of the very small-scale eddies close to the surface can be resolved, which were previously parameterized by the SGS model. This leads also to an increase of the total (SGS+resolved) *TKE* close to the surface.

Our fraction of $e_{\mathrm{SGS}}/e = 31.3\%$ for G06250 is larger than for G06250c (29.2 %, $Q_{\mathrm{S}} = -8.33$ mK m s $^{-1}$) and larger than the value obtained by Jiménez and Cuxart (2005) for their simulations (20.57 % for $u_{\mathrm{g}} = 8$ m s^{-1} and a constant surface heat flux of -10 mK m s $^{-1}$ with a resolution of 6.25 m). This difference might arise as we apply a different SGS scheme in comparison to Jiménez and Cuxart (2005). In addition, we assume that EULAG numerics are more dissipative than the numerics of other solvers due to the nonoscillatory advection scheme MPDATA (see Margolin and Shashkov 2005). This reduces the e_{res} in comparison to e_{SGS}.

5.2 Analysis of the Energy Spectra

For a better understanding of the grid-size influence on the vertical profiles (obtained with the NBA model) as illustrated in Fig. 7, we focus on the intensity of the different turbulent length scales for different values of Δ by analyzing the LES energy spectra. Maronga and Li (2021) hypothesize that a change from 3.125 m to 2 m in grid size leads to a grid-sensitivity caused by large scales. This might be in contrast to Sullivan et al. (2016), who applied and developed (Sullivan et al. 1994), the ANI-SGS model which implies that mainly small-scale

energy differences are responsible for the grid-sensitivity. We will thus analyze in this section the grid sensitivity of both SGS models: the ANI and the NBA model.

In Fig. 8, the horizontal spectra of the total *TKE* density $e(k)$ are displayed for the ANI and the NBA model for all resolutions within this study. They are averaged over the final simulated hour. For the horizontal plane, we choose $z = 50$ m similar to Maronga and Li (2021) (Fig. 9). Larger length scales λ are indicated by smaller values of the wavenumber k and vice versa.

We first focus on the NBA model (solid lines). The finer-resolved spectra of the NBA model simulations (G06250, G03125 and G02000) confirm the findings of Maronga and Li (2021), i.e., a decrease of energy for large scales when moving from 6.25 m to 3.125 m to 2 m resolution. The peak of the G02000 spectrum is positioned at approximately the same length-scale as in Maronga and Li (2021) (Fig. 9). The $e(k)$ of G06250 is larger for $k < 10^{-1}$ m^{-1} than in G03125, but smaller at finer scales. G12500 is overall smaller in turbulence intensity, except for the minimal k value. At the limit of small scales (i.e., the maximum wavenumber of all spectra in Fig. 8), the curvature of the NBA simulations increases and leads to a smaller magnitude of the slope, presumably caused by nonlinear backscattering.

Moving over to the ANI model (dashed lines in Fig. 8), there is also a decrease of $e(k)$ for decreasing grid size observed for all simulations with the exception of G12500. Comparing G06250a with G06250 (orange-dashed with orange line in Fig. 8) shows that both spectra are similar for $k > 10^{-1}$ m^{-1} but that the turbulent energy on larger scales is smaller for the ANI-model. This might explain the different vertical profiles of $e(k)$ in Fig. 6: small-scale, near-surface turbulence can be accurately resolved with the purely dissipative ANI-model, but as no energy backscattering is possible, the energy of the large-scale eddies is too small for a boundary-layer height comparable to the NBA model. The spectral energy density of G03125a and G02000a is smaller over all scales in comparison to G03125 and G02000, with the difference being especially pronounced at the small-scale limit.

In summary, the spectra of the simulations with both the ANI and the NBA SGS model support the findings of Maronga and Li (2021), i.e., that the energy decreases at larger scales

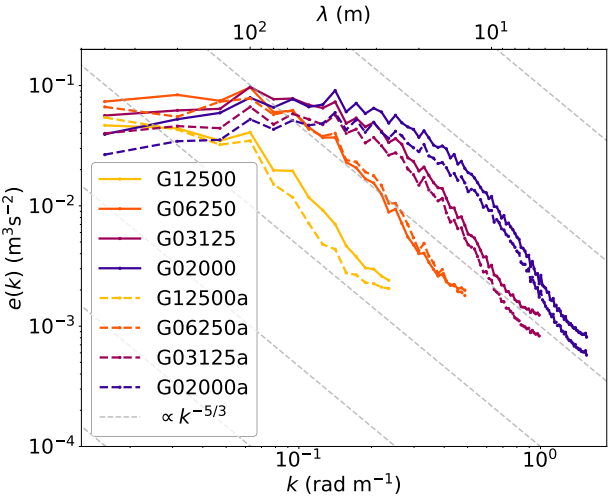

Fig. 8 Horizontal ($z = 50$ m) total *TKE* spectrum averaged over the final simulation hour plotted versus the wave number k and length scale $\lambda = 2\pi k^{-1}$ for simulations with different grid size and with the NBA and the ANI SGS model (see Tab. 1)

for decreasing grid size. For smaller scales, ($k > 10^{-1}$ m^{-1}) an increase of $e(k)$ can be observed for both SGS models.

6 Conclusion and Outlook

The results of SBL-LESs (including the LLJ and the resulting turbulence intensity) are sensitive to the lower boundary condition, the SGS model and the grid size. These sensitivities are investigated using the numerical flow solver EULAG in this study by adapting the widely-used moderately stable boundary layer benchmark case GABLS1. Within our EULAG simulations of the SBL, we prescribe a surface heat flux Q_S continuously varying in time in contrast to studies by Zhou and Chow (2011), who applied a constant surface heat flux over time, and Jiménez and Cuxart (2005), who changed the magnitude of Q_S every two hours. With a prescribed surface heat flux, the surface temperature becomes a variable of the chaotic dynamical system (i.e., subject to turbulence) and is not necessarily predictable. This is different to the other participants of the inter-comparison in Beare et al. (2006) and the studies by Kosović and Curry (2000); Sullivan et al. (2016) and Maronga and Li (2021), who applied a fixed cooling rate.

By prescribing a surface heat flux decreasing with time, a decoupling of the surface temperature is prevented (as compared to a constant heat flux), which would result in rapid cooling and the excessive suppression of turbulence as in Jiménez and Cuxart (2005) and Zhou and Chow (2011). To our knowledge, the reference simulation in this work (G06250 with $\Delta = 6.25$ m, $Q_S = -12.5\sqrt{t/T}$ mK m s^{-1} and the NBA-SGS model) is the first successful attempt to simulate GABLS1 with the surface hfbc, i.e., our results are comparable to the inter-comparison of Beare et al. (2006). Our studies with EULAG and a prescribed surface heat flux were conducted without explicitly using MOST. To further expand our studies in the future, an LES with MOST and a temporal varying surface hfbc might yield more information about the applicability of MOST, in both the wSBL and the vSBL regime.

When applying a surface heat flux constant with time (simulation G06250c), a turbulence regime change is visible with the onset of the LLJ. The trigger mechanisms of SBL regime changes have already been investigated using measurement data (e.g., Sun et al., 2012) or single-column models (e.g., Kaiser et al., 2025). Further LES parameter studies of the SBL and especially the vSBL might expand these regime change investigations.

Varying the SGS model while keeping all other parameters identical leads to differences in turbulent stresses and heat fluxes, in agreement with previous findings by Kosović and Curry (2000). Here, the difference is not only apparent in the mean and turbulent variable profiles, but also in different surface temperatures. For EULAG and 6.25 m, only the NBA model leads to significant continuous turbulence. For the other two tested models, however, excessive cooling leads to an increase in thermal stability and damping of turbulence. Even when adapting the surface heat flux such that all simulations result in the same final surface temperature, the boundary-layer height of the DES and ANI model profiles are too shallow in comparison to the GABLS1 inter-comparison study (Beare et al. 2006). This can partially be understood by the smaller vertical turbulent transport by EULAG relative to other numerical models, caused by EULAG's non-oscillatory advection scheme MPDATA. In addition, MPDATA probably leads to reduced numerical noise in comparison with other numerical flow solvers used in Beare et al. (2006). This noise might help other solvers to

trigger turbulence, while here, nonlinear backscattering is absolutely necessary for continuous turbulence.

We want to highlight that these results and dependencies on the SGS model are subjective to the chosen flow solver EULAG for the investigated spatial resolution of 6.25 m. Successful simulations of the weakly SBL (using a cooling rate as the surface boundary condition and having resolved continuous turbulence) with the ANI model (like Sullivan et al. 2016) exist.

Changing the grid size Δ of the simulations leads to different changes of the mean profiles, depending on the SGS model. The energy spectra showed that for both the NBA and the ANI model, changes in larger-scale turbulence (smaller k) play a significant role, in line with the argumentation of Maronga and Li (2021). We applied here for all simulations the same, constant drag coefficient. As the MOST boundary condition was implemented in EULAG by Englberger et al. (2026), we will for future studies derive a relation between the drag coefficient and the grid size, to potentially reduce grid sensitivity by adapting c_{D} accordingly.

Our simulations were validated only against other simulations of the GABLS1 intercomparison. Future work will compare LES of the SBL with observations to further assess the real-world applicability of the modeling approach analyzed herein. Near-surface measurements of heat fluxes and friction velocity collected by eddy covariance stations are therefore crucial for improving understanding of turbulent mixing in the SBL.

Appendix: Simulations with 2 m Resolution and Decreasing Heat Flux

We briefly discuss the mean profiles and contour plot of the $\Delta = 2$ m simulation G02000 (variational heat flux, NBA SGS model). All settings except for the grid size are identical to G06250 (see Table 1). Figure 9 shows, similar to Fig. 1, the temporal evolution of the mean wind speed and potential temperature, as well as the normalized hodograph. The profiles of G02000 in Fig.9a and b overlap with GABLS1 over all heights. Both the LLJ height as also the temperature inversion height lie on the lower end compared to GABLS1.

Figure 10 shows instantaneous slices over the *xy*- and the *xz*-plane of the resolved wind speed magnitude and $\theta - \theta_{\mathrm{e}}$ of simulation G02000 after nine hours. We investigate whether coherent turbulent structures and temperature fronts are observable using our “benchmark" setup. For a detailed discussion of these structures we direct the reader to Gerz et al. (1994) and Sullivan et al. (2016). As shear and strong temperature gradients are more prominent close to the surface ($z < 50$ m), an altitude of $z = 40$ m is chosen for the *xz*-slices.

The LLJ and the turbulent flow are well visible in Fig. 10a. Figure 10b shows upward tilted temperature fronts below this LLJ. Between $z = 150\mathrm{m}$ and 200m, we observe downward tilted temperature fronts. These results are similar to Sullivan et al. (2016), where the fronts are as well tilted upwards below the LLJ and the tilt angle undergoes a transition to the negative with increasing *z*. The microfronts are also visible in the temperature *xz*-slice (Fig. 10d), the strongest one at $(x, y) = (375$ m, 200 m) and others at (120 m, 70 m) or at

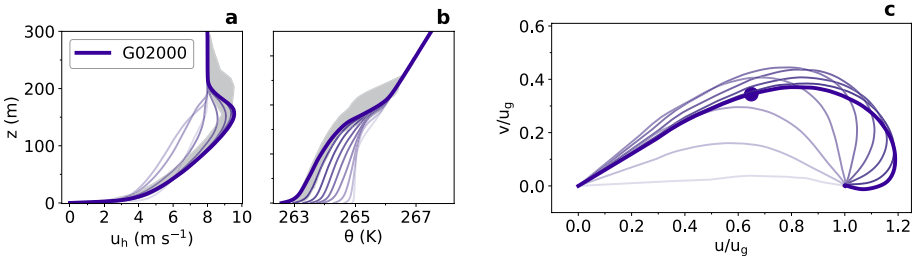

Fig. 9 Thick coloured lines: vertical profiles of (**a**) wind speed and (**b**) potential temperature for G02000 (see Table 1). Hourly profiles are shown by transparent lines, progressing from lighter to darker. The shaded gray area defines the range of profiles of other simulations with the same resolution from Beare et al. (2006). (**c**): normalized hodograph of the simulation. The circle indicates where $z = 40$ m, the height for the contour plots in Fig. 10

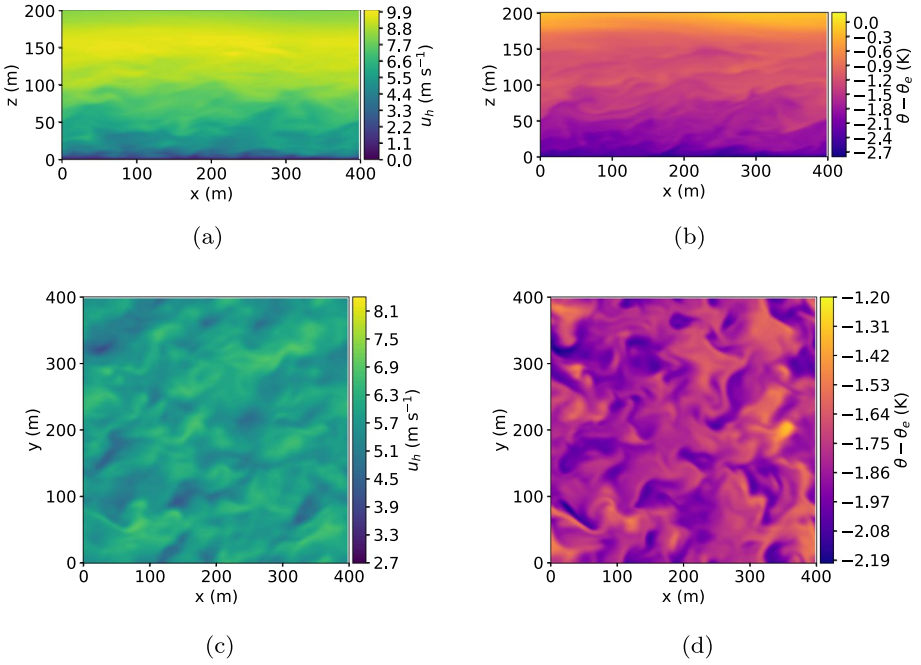

Fig. 10 Contour plots of wind speed (**a**, **c**) and potential temperature fluctuations (**b**, **d**) in the $xz-$ (a, b, $y = 200$ m) and $xy-$ (c, d, $z = 40$ m) plane

(50 m, 290 m). The warm edges of these fronts face the main wind direction of 42° (i.e., approximately to the upper right), similar to Sullivan et al. (2016). Regarding the wind speed xz-slice (Fig. 10c), we see coherent, elongated structures oriented toward the main wind direction induced by the Ekman spiral.

Acknowledgements This research has been funded by the Deutsche Forschungsgemeinschaft (DFG, German Research Foundation) - EN 1357/2-1. All simulations in this publication were conducted at the GCS Supercomputer SuperMUC-NG at Leibniz Supercomputing Centre (LRZ). The authors gratefully acknowledge the Gauss Centre for Supercomputing e.V. (https://www.gauss-centre. eu, last access: 2025/12/20) for

funding this project by providing computing time on the GCS Supercomputer SuperMUC at Leibniz Supercomputing Centre (LRZ, https://www.lrz.de, last access: 2025/12/20). The authors appreciate the valuable feedback and suggestions of both reviewers, which led to significant improvements in the article.

Author Contributions All authors designed the idea. L.B. performed the simulations and wrote the main manuscript text with significant contributions from A.E. . All authors reviewed the manuscript.

Funding Open Access funding enabled and organized by Projekt DEAL.

Data Availability No datasets were generated or analysed during the current study.

Declarations

Conflict of interest The authors declare no Conflict of interest.

References

Beare, et al (2006) An intercomparison of large-eddy simulations of the stable boundary layer. Bound-Layer Meteorol 118(2):247–272. https://doi.org/10.1007/s10546-004-2820-6

Deardorff JW (1980) Stratocumulus-capped mixed layers derived from a three-dimensional model. Bound-Layer Meteorol 18(4):495–527. https://doi.org/10.1007/BF00119502

Englberger A, Dörnbrack A, Smolarkievicz PK, Wyszogrodzki AA (2026) Large-eddy simulations of stably-stratified atmospheric flows: Comparing two lower boundary-condition approaches. In preparation

Epifanio CC (2007) A method for imposing surface stress and heat flux conditions in finite-difference models with steep terrain. Mon Weather Rev 135(3):906–917. https://doi.org/10.1175/MWR3297.1

Galperin B, Sukoriansky S, Anderson PS (2007) On the critical richardson number in stably stratified turbulence. Atmos Sci Lett 8(3):65–69. https://doi.org/10.1002/asl.153

Gerz T, Howell J, Mahrt L (1994) Vortex structures and microfronts. Phys Fluids 6(3):1242–1251. https://doi.org/10.1063/1.868293

Grachev AA, Andreas EL, Fairall CW, Guest PS, Persson POG (2012) The critical richardson number and limits of applicability of local similarity theory in the stable boundary layer. Bound-Layer Meteorol 147(1):51–82. https://doi.org/10.1007/s10546-012-9771-0

Gucci F, Giovannini L, Stiperski I, Zardi D, Vercauteren N (2023) Sources of anisotropy in the reynolds stress tensor in the stable boundary layer. Q J R Meteorol Soc 149(750):277–299. https://doi.org/10.1002/qj.4407

Jiménez MA, Cuxart J (2005) Large-eddy simulations of the stable boundary layer using the standard kolmogorov theory: Range of applicability. Bound-Layer Meteorol 115(2):241–261. https://doi.org/10.1007/s10546-004-3470-4

Kaiser A, Vercauteren N, Krumscheid S (2025) Capturing the variability of the nocturnal boundary layer through localized perturbation modeling. J Atmos Sci 82(1):119–138. https://doi.org/10.1175/jas-d-24-0036.1

Kosović B (1997) Subgrid-scale modelling for the large-eddy simulation of high-reynolds-number boundary layers. J Fluid Mech 336:151–182. https://doi.org/10.1017/S0022112096004697

Kosović B, Curry JA (2000) A large eddy simulation study of a quasi-steady, stably stratified atmospheric boundary layer. Journal of the Atmospheric Sciences

Mahrt L (2014) Stably stratified atmospheric boundary layers. Annu Rev Fluid Mech 46(1):23–45. https://doi.org/10.1146/annurev-fluid-010313-141354

Margolin LG, Shashkov M (2005) MPDATA: gauge transformations, limiters and monotonicity. Int J Numer Meth Fluids 50(10):1193–1206. https://doi.org/10.1002/fld.1070
Maroneze R, Costa FD, Acevedo OC, Medeiros LE, Puhales FS, Anabor V, Mortarini L (2023) A new stable boundary layer parameterization for numerical weather prediction models: A heat flux budget approach. Bound-Layer Meteorol. https://doi.org/10.1007/s10546-023-00810-4
Maronga B, Li D (2021) An investigation of the grid sensitivity in large-eddy simulations of the stable boundary layer. Bound-Layer Meteorol 182(2):251–273. https://doi.org/10.1007/s10546-021-00656-8
McWilliams JC, Meneveau C, Patton EG, Sullivan PP (2023) Stable boundary layers and subfilter-scale motions. Atmosphere 14(7):1107
Peña A, Kosović B, Mirocha JD (2021) Evaluation of idealized large-eddy simulations performed with the weather research and forecasting model using turbulence measurements from a 250 m meteorological mast. Wind Energy Sci 6(3):645–661. https://doi.org/10.5194/wes-6-645-2021
Pope SB (2000) Turbulent Flows. Cambridge University Press. https://doi.org/10.1017/CBO9780511840531
Prusa JM, Smolarkiewicz PK, Wyszogrodzki AA (2008) EULAG, a computational model for multiscale flows. Comput Fluids 37(9):1193–1207. https://doi.org/10.1016/j.compfluid.2007.12.001
Schumann U (1991) Subgrid length-scales for large-eddy simulation of stratified turbulence. Theoret Comput Fluid Dyn 2(5–6):279–290. https://doi.org/10.1007/BF00271468
Schumann U (1995) Stochastic backscatter of turbulence energy and scalar variance by random subgrid-scale fluxes. Proc R Soc Lond A 451(1941):293–318. https://doi.org/10.1098/rspa.1995.0126
Shapiro A, Fedorovich E (2010) Analytical description of a nocturnal low-level jet. Q J R Meteorol Soc 136(650):1255–1262. https://doi.org/10.1002/qj.628
Smolarkiewicz PK, Margolin LG (1997) On forward-in-time differencing for fluids: an eulerian/semi-lagrangian non-hydrostatic model for stratified flows. Atmos Ocean 35(sup1):127–152. https://doi.org/10.1080/07055900.1997.9687345
Smolarkiewicz PK, Margolin LG (1998) MPDATA: A finite-difference solver for geophysical flows. J Comput Phys 140(2):459–480. https://doi.org/10.1006/jcph.1998.5901
Stoll R, Gibbs JA, Salesky ST, Anderson W, Calaf M (2020) Large-eddy simulation of the atmospheric boundary layer. Bound-Layer Meteorol 177(2–3):541–581. https://doi.org/10.1007/s10546-020-00556-3
Stull RB (1988) An Introduction to Boundary Layer Meteorology. Springer Netherlands. https://doi.org/10.1007/978-94-009-3027-8
Sullivan PP, McWilliams JC, Moeng CH (1994) A subgrid-scale model for large-eddy simulation of planetary boundary-layer flows. Bound-Layer Meteorol 71(3):247–276. https://doi.org/10.1007/BF00713741
Sullivan PP, Weil JC, Patton EG, Jonker HJJ, Mironov DV (2016) Turbulent winds and temperature fronts in large-eddy simulations of the stable atmospheric boundary layer. J Atmos Sci 73(4):1815–1840. https://doi.org/10.1175/JAS-D-15-0339.1
Sun J, Mahrt L, Banta RM, Pichugina YL (2012) Turbulence regimes and turbulence intermittency in the stable boundary layer during cases-99. J Atmos Sci 69(1):338–351. https://doi.org/10.1175/JAS-D-11-082.1
Zhou B, Chow FK (2011) Large-eddy simulation of the stable boundary layer with explicit filtering and reconstruction turbulence modeling. J Atmos Sci 68(9):2142–2155. https://doi.org/10.1175/2011JAS3693.1